

**Hard-photon flow and photon-photon correlation in intermediate-energy heavy-ion collisions**

Y. G. Ma (马余刚),\* G. H. Liu (刘桂华), X. Z. Cai (蔡翔舟), D. Q. Fang (方德清), W. Guo (郭威), W. Q. Shen (沈文庆), W. D. Tian (田文栋), and H. W. Wang (王宏伟)

*Shanghai Institute of Applied Physics, Chinese Academy of Sciences, Shanghai 201800, China*

(Received 2 August 2011; revised manuscript received 25 January 2012; published 24 February 2012)

Hard photons emitted from energetic heavy-ion collisions are very interesting since they do not experience nuclear interaction, and therefore they are useful to explore properties of nuclear matter. We investigated hard-photon production and its properties in intermediate-energy heavy-ion collisions with the help of the Blotzmann-Uehling-Ulenbeck model. Two components of hard photons are discussed: direct and thermal. The positive directed flow parameter and negative elliptic flow parameter of direct photons are demonstrated and they are anticorrelated to the flows of free protons. The dependencies of hard-photon production and anisotropic parameters on impact parameter, beam energy, nuclear equation of state, and symmetry energy are also discussed. Furthermore, we investigated the two-photon momentum correlation function, from which the space-time structure information of the photon source could be extracted, as well as the two-photon azimuthal correlation, which could provide another good method to determine the elliptic flow parameter  $v_2$  of direct hard photons.

DOI: [10.1103/PhysRevC.85.024618](https://doi.org/10.1103/PhysRevC.85.024618)

PACS number(s): 25.75.Ld, 24.10.-i, 21.60.Ka, 25.70.-z

**I. INTRODUCTION**

One of the main goals of intermediate-energy heavy-ion collision (HIC) is to study properties of nuclear matter, especially to determine the nuclear equation of state (EOS). HIC provides a unique means to compress nuclear matter to a hot and dense phase within a laboratory environment. The pressures that result from the high densities achieved during such collisions strongly influence the motion of ejected matter and are sensitive to the EOS. In comparison with conventional hadronic probes, photons interacting only weakly through the electromagnetic force with the nuclear medium are not subjected to distortions by the final-state (neither Coulomb nor strong) interactions and therefore photon delivers an undistorted picture of the emitting source [1–4].

During the past two decades, many model calculations and experimental facts [1–9] have indicated that in intermediate-energy heavy-ion collisions hard photons (defined as photons with energies above the giant dipole resonance domain, above 30 MeV in this paper) mainly originate from incoherent proton-neutron bremsstrahlung collisions, namely,  $p + n \rightarrow p + n + \gamma$ . A nice review paper on hard photon is available [3]. These hard photons are emitted from two distinct sources. The first and dominant component, denoted as a direct hard photon (called a “direct photon” for short), is associated with the first-chance proton-neutron collisions in the initial phase of the heavy-ion reaction. The second one, originating from the secondary proton-neutron collisions in the later stage of the reactions when the dinuclear system tends to be thermalized, is accordingly called a thermal hard photon (or a “thermal photon” for short). Because of their distinct emission sources, direct photons and thermal photons can deliver thermodynamic and dynamical information of hot and dense nuclear matter formed during the various stages of heavy-ion collisions.

In relativistic heavy-ion collisions, photons are also of very interesting since they can serve as one of the potential signals of quark-gluon plasma (QGP) formation (e.g., see Ref. [10–13]). A hot QGP radiates a large amount of thermal photons, which dominate the spectra at small transverse momenta, whereas hard processes in nucleon-nucleon scatterings produce large-momenta photons. Therefore photon enhancement at low transverse momenta could be seen as a QGP signal, which has been observed at the BNL Relativistic Heavy-Ion Collider [10]. Similar to the feature of photon production in intermediate-energy HIC, photons emitted from the interior of the hot matter no longer interact with the hadronic medium, in contrast to hadronic observables.

The paper is organized as follows. In Sec. II, the simulation tool which we used is briefly introduced and the calculation method of photon production is outlined. Section III describes the classification of hard photons and the definition of anisotropic flow and presents the results of the azimuthal asymmetry for direct photons and free protons. In Sec. IV, we discuss the different variables (impact parameter, beam energy, and EOS) dependencies of hard-photon production and/or anisotropic flow parameters. Section V gives the results and discussions on two-photon correlation functions, namely, the momentum correlation function, which is also called the Hanbury-Brown and Twiss (HBT) correlation function, as well as the azimuthal correlation function. Finally, a summary is given in Sec. VI.

**II. BRIEF INTRODUCTION TO THE MODEL AND PHOTON PRODUCTION****A. The Blotzmann-Uehling-Ulenbeck equation**

The transport model is very useful for treating heavy-ion collision dynamics and obtaining important information on nuclear matter. In intermediate-energy heavy-ion collisions, the Blotzmann-Uehling-Ulenbeck (BUU) model is an extensively

\* [ygma@sinap.ac.cn](mailto:ygma@sinap.ac.cn)

useful tool [14]. The BUU equation, which takes both Pauli blocking and the mean field into consideration, reads

$$\begin{aligned} & \frac{\partial f}{\partial t} + v \cdot \nabla_r f - \nabla_r U \cdot \nabla_p f \\ &= \frac{4}{(2\pi)^3} \int d^3 p_2 d^3 p_3 d\Omega \frac{d\sigma_{NN}}{d\Omega} V_{12} \times [f_3 f_4 (1-f)(1-f_2) \\ & \quad - f f_2 (1-f_3)(1-f_4)] \delta^3(p+p_2-p_3-p_4). \end{aligned} \quad (1)$$

It is solved with the method of Bertsch and Das Gupta [15]. In Eq. (1),  $\frac{d\sigma_{NN}}{d\Omega}$  and  $V_{12}$  are the in-medium nucleon-nucleon cross section and the relative velocity for the colliding nucleons, respectively, and  $U$  is the mean-field potential including the isospin-dependent term:

$$U(\rho, \tau_z) = a \left( \frac{\rho}{\rho_0} \right) + b \left( \frac{\rho}{\rho_0} \right)^\sigma + C_{\text{sym}} \frac{(\rho_n - \rho_p)}{\rho_0} \tau_z, \quad (2)$$

where  $\rho_0$  is the normal nuclear matter density;  $\rho$ ,  $\rho_n$ , and  $\rho_p$  are the nucleon, neutron, and proton densities, respectively; and  $\tau_z$  equals 1 or  $-1$  for neutrons and protons, respectively. The coefficients  $a$ ,  $b$ , and  $\sigma$  are parameters for the nuclear equation of state. Three sets of mean-field parameters are used, namely, the soft EOS with a compressibility  $K$  of 200 MeV ( $a = -356$  MeV,  $b = 303$  MeV,  $\sigma = 7/6$ ), the semisoft EOS with  $K$  of 235 MeV ( $a = -218$  MeV,  $b = 164$  MeV,  $\sigma = 4/3$ ), and the hard EOS with  $K$  of 380 MeV ( $a = -124$  MeV,  $b = 70.5$  MeV,  $\sigma = 2$ ).  $C_{\text{sym}}$  is the symmetry energy strength due to the density difference of neutrons and protons in the nuclear medium. Although  $C_{\text{sym}}$  is important for asymmetrical nuclear matter (here  $C_{\text{sym}} = 32$  MeV is used), it is trivial for the symmetric system studied in the present work.

### B. Production cross sections of bremsstrahlung hard photons

The BUU model was shown to be very successful in describing the bulk properties of the reaction and nucleon emission in intermediate-energy heavy-ion collisions. In addition, the proton-neutron bremsstrahlung photon can be simulated as well in the model. For determining the elementary double-differential hard-photon production cross sections on the basis of individual proton-neutron bremsstrahlung, the hard-sphere collision was adopted from Ref. [16] and modified as in Ref. [17] to allow for energy conservation. The double differential probability is given by

$$\frac{d^2\sigma^{\text{elem}}}{dE_\gamma d\Omega_\gamma} = \alpha_c \frac{R^2}{12\pi} \frac{1}{E_\gamma} (2\beta_f^2 + 3\sin^2\theta_\gamma \beta_i^2). \quad (3)$$

Here  $R$  is the radius of the sphere,  $\alpha_c$  is the fine-structure constant,  $\beta_i$  and  $\beta_f$  are the initial and final velocity of the proton in the proton-neutron center-of-mass system, and  $\theta_\gamma$  is the angle between the incident proton direction and the photon emitting direction. More details for the model can be found in Refs. [14,18].

## III. AZIMUTHAL ASYMMETRY OF HARD PHOTONS

### A. Definitions of direct photons and thermal photons

In the present work, we simulate  $^{40}\text{Ca} + ^{40}\text{Ca}$  collisions in most cases. Sometimes  $^{48}\text{Ca} + ^{48}\text{Ca}$  and  $\text{Kr} + \text{Ni}$  collisions are also simulated.

Figures 1(a) and 1(b) show the time evolutions of the production rate of bremsstrahlung hard photons and of system densities, including both maximum density (closed circles) and average density (open circles), respectively, for  $^{40}\text{Ca} + ^{40}\text{Ca}$  collisions at 60A MeV in the centrality of 40%–60%. It is found that the hard-photon production rate is sensitive to the density oscillations during the whole reaction evolution. With the increase in density when the collision system is in the compression stage, the system produces more hard photons. In contrast, when the system starts to expand, the hard-photon production rate decreases. Actually, the density oscillation of the colliding heavy-ion systems can be observed in the experiments via hard-photon interferometry measurements [1,6,19] as well as dynamical dipole  $\gamma$  radiation [20–22]. Apparently, hard photons are mostly produced at the early stage of the reaction. Thereafter we call these photons, emitted before the time of the first maximum expansion of the system ( $t \sim 65$  fm/c in Ca + Ca at 60A MeV), direct hard photons [on the left side of the blue dashed line in Fig. 1(a)]. It is also coincident with the definition in Sec. I of direct hard photons. We call the residual hard photons produced in the later stage thermal hard photons (on the right side of the blue dashed line in Fig. 1). In this way, we can identify the producing photon as either direct or thermal by the emission time of photons in the present simulation. We notice that the production rate of thermal photons tends to decrease for later time, after 300 fm/c for Ca + Ca at 60A MeV, which can be understood by the decrease of  $n$ - $p$  collisions in an expanding system. However, the hard-photon yields in the later stage after 300 fm/c are a relatively small fraction of the total thermal hard-photon emission. Also, in the following calculations, we mainly focus

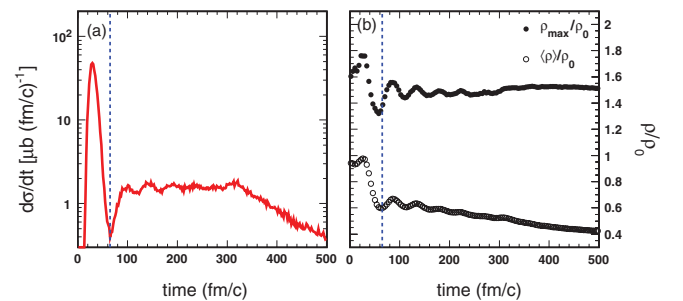


FIG. 1. (Color online) (a) Time evolution of hard-photon production rate for the reaction  $^{40}\text{Ca} + ^{40}\text{Ca}$  at 60A MeV in 40%–60% centrality. The EOS parameters with an compressibility  $K$  of 235 MeV are used. (b) Time evolution of reduced maximum density  $\rho_{\text{max}}/\rho_0$  (closed circles) and reduced average density  $\langle\rho\rangle/\rho_0$  (open circles) of the whole reaction system in the same reaction. The blue dashed line represents the time when till the first expansion stage, and in the panel (a) it separates direct hard photons (on the left side) and thermal hard photons (on the right side).

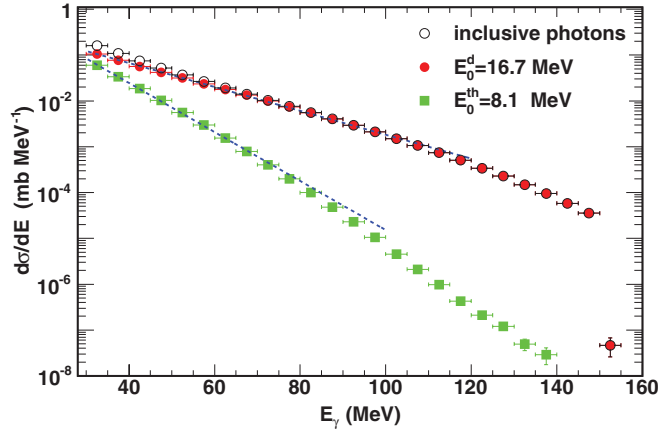


FIG. 2. (Color online) Kinetic energy spectrum of direct photons and thermal photons for inclusive events of  $^{40}\text{Ca} + ^{40}\text{Ca}$  at 60A MeV with compressibility an  $K$  of 235 MeV. Black dots and blue dots represent the direct photons and thermal photons, respectively. Lines represent the exponential fits with Eq. (5).

on direct hard photons, which dominate the yield and do not depend on the time evolution for the later stage.

For an example, Fig. 2 demonstrates that the direct and thermal hard photons for 60A MeV  $^{40}\text{Ca} + ^{40}\text{Ca}$  collisions with a compressibility  $K$  of 235 exhibit different spectral shapes: thermal photons give rise to a softer energy spectrum than direct ones. In the nucleon-nucleon center-of-mass system, the photon spectrum can be described by the function

$$\frac{d\sigma}{dE_\gamma} = I_0 e^{-\frac{E_\gamma}{E_0}}, \quad (4)$$

where  $I_0$  is a normalization constant and  $E_0$  is the slope parameter, which reflects the apparent source temperature of the photon emission source. The slope parameter  $E_0$  depends on the bombarding energy and on the average intrinsic momentum of the participant nucleons. As less energy is available on average in second-chance  $n$ - $p$  collisions than in first-chance collisions because most of the projectile kinetic energy is damped, the thermal-photon spectrum becomes much softer. If one adds the two sources together in the photon spectrum, one obtains an empirical photon spectrum of the form [1,8,9]

$$\frac{d\sigma}{dE_\gamma} = K_d e^{-\frac{E_\gamma}{E_0^d}} + K_{th} e^{-\frac{E_\gamma}{E_0^{th}}}, \quad (5)$$

with the constant  $K_{d,th}$  defined by

$$I_{d,th} = K_{d,th} \int_{E_{30}}^{\infty} e^{-\frac{E_\gamma}{E_0^{d,th}}} dE_\gamma = K_{d,th} E_0^{d,th} e^{-\frac{E_{30}}{E_0^{d,th}}}. \quad (6)$$

$I_{d,th}$  represents the intensity of each photon source,  $d$  stands for the direct photon, and  $th$  for stands for the thermal photon. However, we notice that the change in slope of the photon yield could be also affected by the  $1/E_\gamma$  factor which enters the elementary  $np - np\gamma$  bremsstrahlung probability [23]. In this case, Eq. (5) should be changed into

$$\frac{d\sigma}{dE_\gamma} = \frac{(K_d)'}{E_\gamma} e^{-\frac{E_\gamma}{(E_0^d)'}} + \frac{(K_{th})'}{E_\gamma} e^{-\frac{E_\gamma}{(E_0^{th})'}}. \quad (7)$$

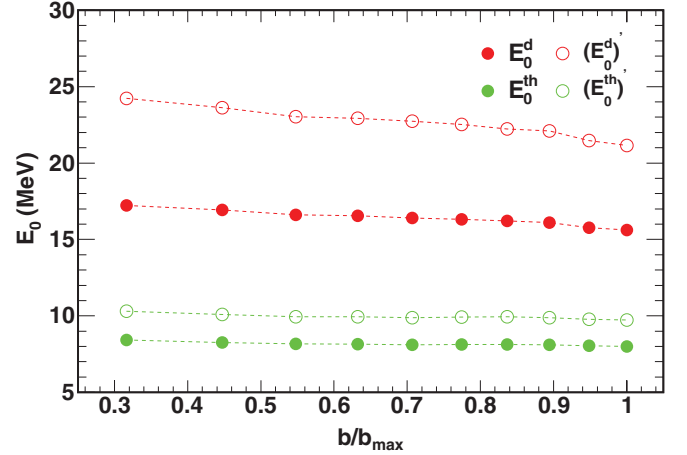


FIG. 3. (Color online) The slope parameters of direct and thermal hard photons as a function of impact parameter for  $^{40}\text{Ca} + ^{40}\text{Ca}$  at 60A MeV with an incompressibility  $K$  of 235 MeV. Open symbols represent the results from the Eq. (7) and solid symbols are from Eq. (5).

In the next paragraph, we will compare the difference for the fitted slope with Eqs. (5) and (7).

As shown in the inset of the figure, the slope parameters of direct photons and thermal photons are 16.7 and 8.1 MeV, respectively, for inclusive events of  $^{40}\text{Ca} + ^{40}\text{Ca}$  collisions at 60A MeV with an incompressibility  $K$  of 235 MeV if we fit the spectrum with Eq. (5). However, Eq. (7) will give larger slope values, namely, 22.5 and 9.8 MeV, respectively, which is 35% and 20% higher than the fits without the  $1/E_\gamma$  factor (not plotted in the figure). With two different fit formulas, we put the impact parameter dependence of the slope parameter together in Fig. 3. A remarkable difference is seen between the slope values with and without the  $1/E_\gamma$  factor; i.e., Eq. (7) gives a higher apparent photon temperature than Eq. (5). In some previous experimental analyses [1,8,9], Eq. (5) was mostly used to extract the apparent slope, but this is probably not correct since a factor  $1/E_\gamma$  in front of the exponential form can be derived from their elementary cross sections [see Eq. (3)]. On the other hand, the slope of hard photons displays a slight decreasing behavior with increasing impact parameter, indicating that the emission source becomes cooler in peripheral collisions. Moreover, direct photons are hotter than thermal photons, as we expected.

## B. Definition of anisotropic flows

It is well known that collective flow is an important observable in heavy-ion collisions and it can carry some essential information on nuclear matter, such as the nuclear equation of state [24–34]. Anisotropic flows are defined as different  $n$ th harmonic coefficients  $v_n$  of an azimuthal Fourier expansion of the particle invariant distribution [25]:

$$\frac{dN}{d\phi} \propto 1 + 2 \sum_{n=1}^{\infty} v_n \cos(n\phi), \quad (8)$$

where  $\phi$  is the azimuthal angle between the transverse momentum of the particle and the reaction plane. Note that in the coordinate system the  $z$  axis is along the beam axis, and the impact parameter axis is labeled as the  $x$  axis.

The first harmonic coefficient  $v_1$  represents the directed flow,

$$v_1 = \langle \cos \phi \rangle = \left\langle \frac{p_x}{p_t} \right\rangle, \quad (9)$$

where  $p_t = \sqrt{p_x^2 + p_y^2}$  is the transverse momentum. The second harmonic coefficient  $v_2$  represents the elliptic flow, which characterizes the eccentricity of the particle distribution in momentum space,

$$v_2 = \langle \cos(2\phi) \rangle = \left\langle \frac{p_x^2 - p_y^2}{p_t^2} \right\rangle. \quad (10)$$

### C. Directed and elliptic flows of direct photons and free protons

In relativistic heavy-ion collisions directed and elliptic flows of hard photons have been recently reported in experiments and through theoretical calculations [35–39], demonstrating a very useful tool for exploring the properties of hot dense matter. However, there are no experimental data available so far on the flow of hard photons in intermediate-energy heavy-ion collisions. In this context, here we calculate directed transverse or elliptic flows in intermediate-energy heavy-ion collisions. In addition, given that hard photons mostly originate from bremsstrahlung by individual proton-neutron collision and that free nucleons are also emitted from nucleon-nucleon collisions, therefore it will be interesting to compare flows of protons and photons.

Figure 4 shows the time evolution of the average values of directed flow and elliptic flow of photons. Considering the nearly symmetric behavior for directed flow versus rapidity, here we calculate the average  $v_1$  over only the positive rapidity range, which can be taken as a measure of the directed flow.

From Fig. 4, the directed flow of photons rises rapidly with positive values during the compression stage and later on it decreases to even a negative value. Afterward, the directed flow remains negative since the system is never compressed. For elliptic flow, the behavior shows a contrary trend to that of  $v_1$  and, later, it shows oscillation for thermal-photon emission. The times corresponding to the peak or valley values of flows roughly keep synchronized with the compression or expansion oscillation of the system evolution as shown in Fig. 1(b).

From the above calculations, we learn that direct photons are preferentially emitted in the out-of-plane (negative  $v_2$ ) direction and thermal photons are emitted from a thermalizing system which makes their emission more isotropic (i.e., the oscillated elliptic flow) than the direct ones produced in the preequilibrium stage. In addition, thermal photons contribute less than 30% of the total yield of hard photons in the present model. Therefore we will focus on direct hard photons to discuss the flow results.

The quantity of directed transverse flow at mid-rapidity can be also defined by the slope:  $F = \frac{d\langle p_x \rangle}{d(y)_{c.m.}}|_{(y)_{c.m.}=0}$ , where  $(y)_{c.m.}$  is the rapidity of particles in the center-of-mass (c.m.) system

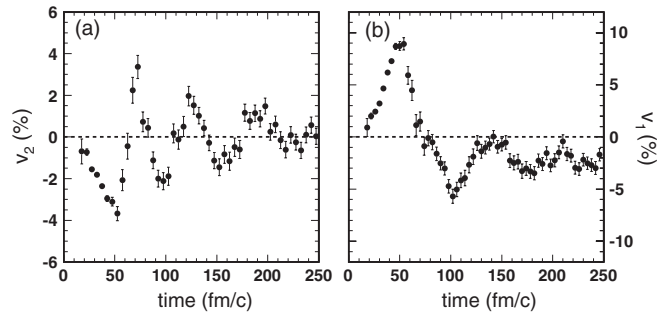


FIG. 4. The time evolution of elliptic flow ( $v_2$ ) of hard photons (a) and directed flow ( $v_1$ ) (b) for 60A MeV Ca + Ca collisions at centrality of 40–60%.

and  $\langle p_x \rangle$  is the mean in-plane transverse momentum of photons or protons in a given rapidity region. In Figs. 5(a) and 5(b), we show  $\langle p_x \rangle$  plotted versus the c.m. rapidity  $y_{c.m.}$  for direct hard photons (a) as well as  $\langle p_x \rangle$  plotted versus the reduced c.m. rapidity  $(y/y_{beam})_{c.m.}$  for free protons (b) for 60A MeV Ca + Ca collisions in the semicentral centrality of 40%–60%. The EOS parameters with a compressibility  $K$  of 235 MeV are used. The errors shown are only statistical. For an emitted proton (free proton), we identify it in the BUU calculation as its local density  $\rho < 1/8\rho_0$ . We take the values of flows when the system has already been in the freeze-out time at 180 fm/c. A good linearity is seen in the mid-rapidity region ( $-0.5, 0.5$ ) and the slope of a linear fit can be defined as the magnitude of directed transverse flow. The extracted value for the directed transverse flow of direct hard photons is about +3.9 MeV/c, and that of free protons is about  $-23.7$  MeV/c. Thus direct hard photons do exist in the directed transverse flow even though the absolute value is smaller than the proton's flow, and the sign of its flow is just opposite to that of free protons.

In order to extract the value of elliptic flow and reduce the error of fits, we fit the azimuthal distribution to a fourth-order Fourier expansion. Figure 6 shows an example for such fits with the elliptic flow parameters  $v_2 = -2\%$  for photons and  $v_2 = 5.5\%$  for protons.

Figure 7 shows the differential elliptic flow of direct hard photons (a) and of free protons (b) as a function of transverse

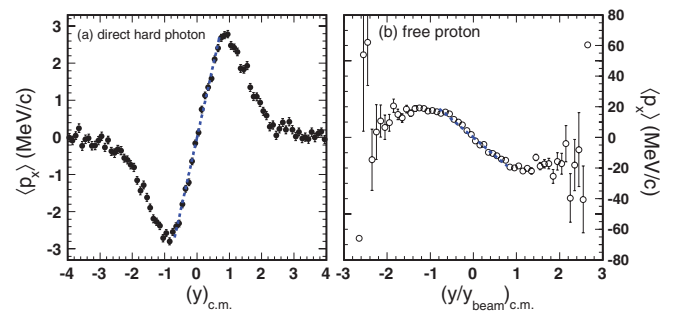


FIG. 5. (Color online) (a) Average in-plane transverse momentum of direct hard photons as a function of c.m. rapidity for 60A MeV Ca + Ca collisions in the semicentral centrality of 40%–60%. The dashed line segment is a fit over the mid-rapidity region  $-0.5 \leq y_{c.m.} \leq 0.5$ . (b) Same as the left panel but for free protons. The dashed line segment is a fit over the mid-rapidity region  $-0.5 \leq (y/y_{beam})_{c.m.} \leq 0.5$ .



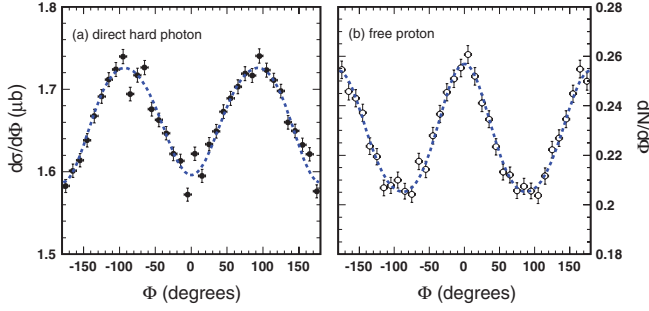


FIG. 6. (Color online) The azimuthal distribution of (a) direct photons and of (b) free protons for 60A MeV Ca + Ca collisions in the semicentral centrality of 40%–60%. Both distributions are fitted to a fourth-order Fourier expansion.

momentum  $p_T$  for  $^{40}\text{Ca} + ^{40}\text{Ca}$  collisions at 60A MeV. Similar to the directed transverse flow, the values of elliptic flow of direct hard photons and of free protons also have opposite signs at this reaction energy, i.e., reflecting a different preferential transverse emission in the out-of-plane or in-plane direction, respectively. Meanwhile, absolute flow values for photons are smaller than the proton's, like the behavior of transverse flow. Except for the opposite sign, we see that both elliptic flows have similar tendency with increasing  $p_T$ ; i.e., their absolute values increase at lower  $p_T$  and become gradually saturated, especially for direct hard photons.

To explain this correlation of the collective flow between direct hard photons and free protons, we should note that flows of direct hard photons originate from individual proton-neutron collisions. As Eq. (3) shows, we can roughly consider that in the individual proton-neutron c.m. system, in directions perpendicular to the incident proton velocity, i.e.,  $\theta_\gamma = 90^\circ$ , the probability of hard-photon production is much larger than in the parallel direction; actually, it is also in agreement with theoretical calculations and with experiments [40,41]. As a whole, the flow of hard photons should be correlated with the collective movement of the nucleons, and it presents an opposite behavior. Consequently, flows of hard photons and of free nucleons exhibit opposite character.

#### IV. DEPENDENCIES OF HARD-PHOTON PRODUCTION AND FLOW ON SOME VARIABLES

##### A. Impact parameter dependence

It is well known that anisotropic flow mainly originates from the initial asymmetric overlap zone of colliding nuclei which induces different pressures or rotational collective motion of the participant region and leads to anisotropic emission of particles. Peripheral collisions have more initial asymmetry in the overlap zone than do central collisions, and thus more anisotropic particle emission is expected. Therefore anisotropic emission should be sensitive to impact parameter.

Here we simulate  $^{40}\text{Ca} + ^{40}\text{Ca}$  collisions at 60A MeV and use the EOS parameters with a compressibility  $K$  of 235 MeV for the nuclear mean field  $U$ . Figures 8(a) and 8(b) show the directed transverse flow parameter  $F$  of direct photons and free protons, respectively, as a function of the reduced

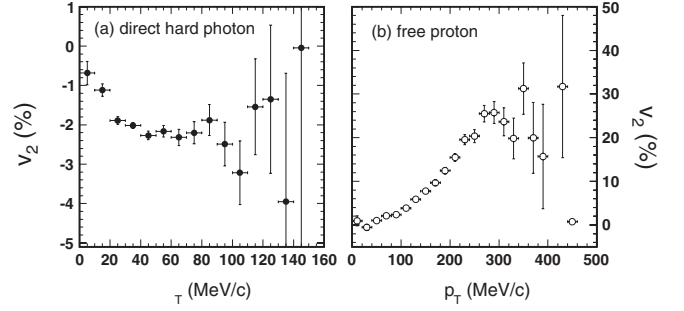


FIG. 7. Elliptic flows ( $v_2$ ) for direct hard photons (a) and free protons (b) as a function of transverse momentum ( $p_T$ ) for 60A MeV Ca + Ca collisions in the semicentral centrality of 40%–60%.

impact parameter (i.e., normalized by the maximum impact parameter). Figures 8(c) and 8(d) are the same as (a) and (b) but for the elliptic asymmetry coefficient  $v_2$ . We can see that both  $F$  and  $v_2$  of direct photons and free protons have similar tendency with impact parameter; i.e., their absolute values increase with the impact parameter except for the slight decrease in very peripheral collisions for  $v_2$ . We also see that, at all impact parameters, in contrast to the negative directed transverse flow and positive elliptic flow of free protons, direct photons show positive  $F$  and negative  $v_2$ ; i.e., the anisotropy is shifted by a phase of  $\pi/2$ . This agrees with the previous conclusion that the azimuthal asymmetry of direct photons is anticorrelated with the corresponding free proton flow.

##### B. Beam energy dependence

In Fig. 9 we show the directed transverse flow parameter  $F$  and elliptic asymmetry coefficient  $v_2$  of direct photons and free protons, respectively, as a function of beam energy for Ca + Ca collisions at (40%–60%) centrality. In the beam energy range studied here, as with the impact parameter dependence, the opposite signs of  $F$  and  $v_2$  between direct photons and free protons are also anticorrelated. Moreover, except for the opposite sign, the directed transverse flow parameter  $F$  of direct photons and free protons have similar structures

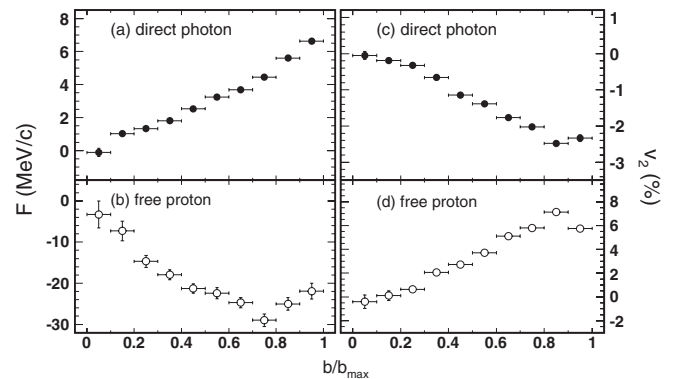


FIG. 8. Directed transverse flow parameter  $F$  of (a) direct photons and (b) free protons, respectively, as a function of the reduced impact parameter for  $^{40}\text{Ca} + ^{40}\text{Ca}$  collisions at 60A MeV. (c) and (d) Same as (a) and (b) but for elliptic asymmetry coefficient  $v_2$ .

with increasing beam energy. The value of the direct-photon elliptic asymmetry coefficient  $v_2$  increases with beam energy from negative to positive, a tendency similar to available experimental results on hard photons in relativistic heavy-ion collisions.

### C. EOS and symmetry energy dependencies

In this section we will discuss the nuclear equation of state and its symmetry energy term dependencies of hard-photon production. In our calculations, the single-particle potential taken as the Skyrme parametrized mean-field potential including the symmetry potential is

$$U^{n(p)}(\rho) = \alpha \left( \frac{\rho}{\rho_0} \right) + \beta \left( \frac{\rho}{\rho_0} \right)^\sigma + V_{\text{asy}}^{n(p)}(\rho, \delta), \quad (11)$$

where the coefficients  $a$ ,  $b$ , and  $\sigma$  are parameters for the nuclear equation of state, which is determined by the nuclear saturation property and the incompressibility  $K$  of symmetric nuclear matter;  $\delta$  is the isospin-asymmetry parameter,  $\delta = (\rho_n - \rho_p)/(\rho_n + \rho_p)$ , and  $V_{\text{asy}}^{n(p)}(\rho, \delta)$  is the symmetry potential of neutrons (protons).

First, we only investigate the effects of the incompressibility  $K$  on hard-photon production in the symmetric reaction system. In the Skyrme potential, we take the incompressibility  $K$  as 200, 235, and 380 MeV, in which the first two correspond to soft and semisoft potentials and the last one corresponds to the hard potential we introduced in Sec. II A.

Because of the sensitivity to the density oscillations of the colliding system, hard photons should be also dependent on the EOS of nuclear matter, especially for thermal hard photons [6,7]. Actually, as shown in Fig. 10, photon production shows its sensitivity to the compressibility, especially for thermal photons, which are produced after  $t \sim 80$  fm/c. The figure shows that the stiffer the EOS is, the higher is the multiplicity of the thermal photons. In contrast, direct photons are produced by the first-channel neutron-proton bremsstrahlung; their production rate only weakly depends on the EOS since direct hard photons are emitted by the

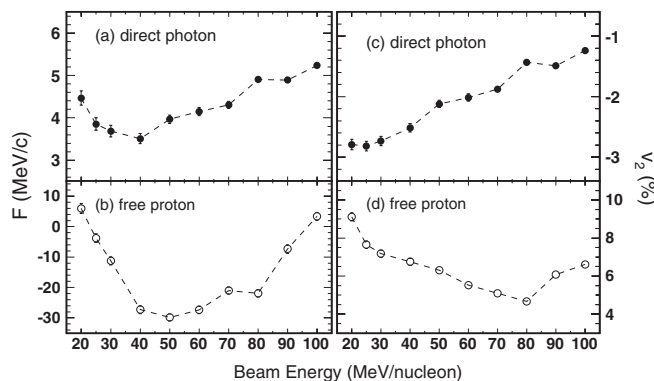


FIG. 9. Directed transverse flow parameter  $F$  of (a) direct photons and (b) free protons, respectively, as a function of beam energy for the reaction which is the same as Fig. 8 but for only semicentral events (40%–60%). (c) and (d) Same as (a) and (b) but for elliptic asymmetry coefficient  $v_2$ .

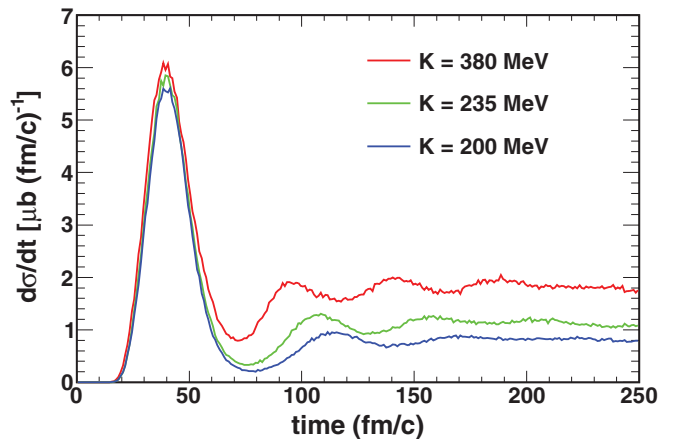


FIG. 10. (Color online) Time evolution of the production rate of bremsstrahlung photons for inclusive events of  $^{40}\text{Ca} + ^{40}\text{Ca}$  at 30A MeV. Different equations of state are used, namely, the hard EOS, the semisoft EOS, and the soft EOS, respectively.

first-channel  $n$ - $p$  scattering when the system is in a highly nonequilibrium state during the compression stage, and they do not have enough time to feel the EOS.

Shown in Fig. 11 is the time evolution of inclusive hard-photon multiplicity from the symmetric reaction system  $^{40}\text{Ca} + ^{40}\text{Ca}$  at 60A MeV. We can see that at this energy, for different incompressibility  $K$ , multiplicities of hard photons produced in the early stage of collisions are nearly equivalent and later they show a clear correlation with incompressibility  $K$ . Corresponding to direct and thermal photons, this indicates that direct-photon production is not sensitive to incompressibility  $K$ , because, at this reaction energy, comparable with two-body interactions, the mean field can be neglected in producing hard photons in the early stage of collisions. However, there is a correlation between  $K$  and thermal-photon production, with larger  $K$  producing more thermal photons.

For the magnitude of flow parameters  $F$  and  $v_2$ , comparisons are made for different equations of state. Figure 12 shows  $F$  and  $v_2$  as a function of impact parameter with different equations of state. Generally, the directed flow becomes larger

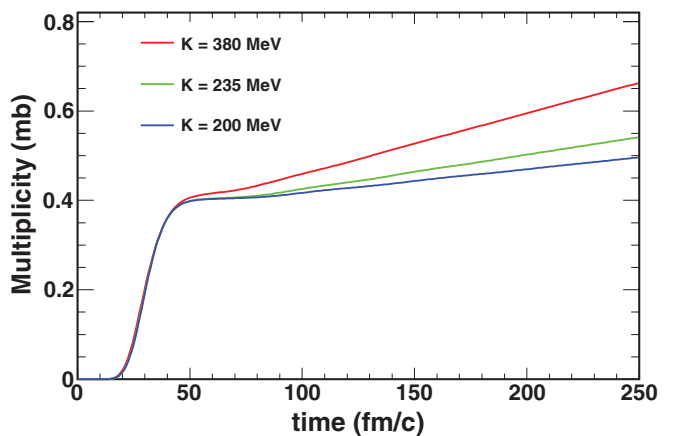


FIG. 11. (Color online) Time evolution of hard-photon multiplicity with different incompressibility  $K$  for the reaction  $^{40}\text{Ca} + ^{40}\text{Ca}$  at 60A MeV.

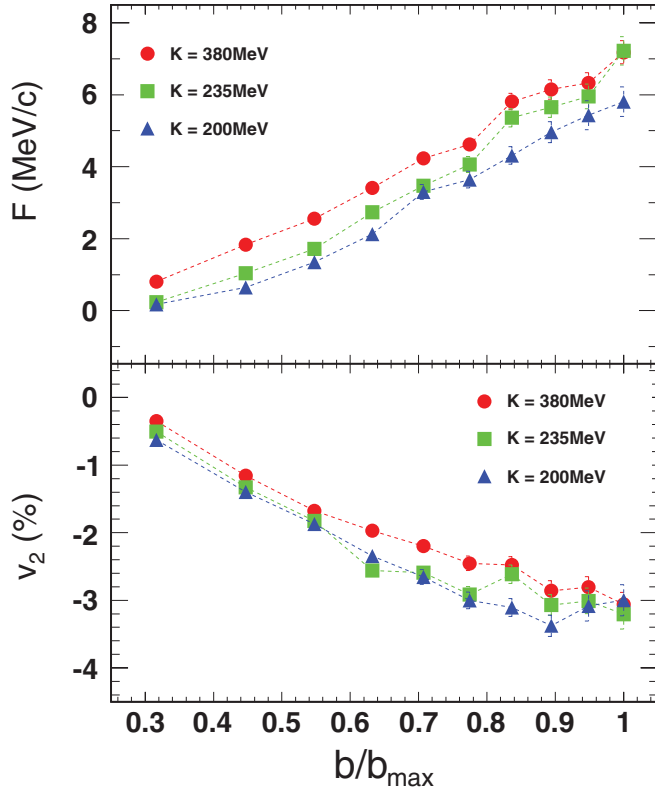


FIG. 12. (Color online) Directed flow parameter ( $F$ ) and elliptic flow ( $v_2$ ) as a function of impact parameter with different EOS parameters for Ca + Ca at 30A MeV.

with the increasing of stiffness of the EOS, whereas the elliptic flow becomes smaller.

In order to study the effects of the symmetry potential, we now set the incompressibility  $K$  to 380 MeV. We mainly consider three kinds of symmetry potential: (1) the case where the symmetry potential is neglected, that is,

$$V_{\text{asy}}^{(0)}(\rho, \delta) = 0; \quad (12)$$

(2) the case where the symmetry potential is a linear function of the isospin-asymmetry parameter  $\delta$ , that is,

$$V_{\text{asy}}^{(1)}(\rho, \delta) = C_{\text{sym}} \delta \tau^{n(p)}, \quad (13)$$

where  $C_{\text{sym}} = 32$  MeV,  $\tau^n = 1$ , and  $\tau^p = -1$ ; and

(3) the Li *et al.* single-particle symmetry potential from the parametrization of nuclear symmetry energy used in Ref. [42] for studying the properties of neutron stars, that is,  $E_{\text{sym}}(\rho) = E_0(\rho_0)(\frac{\rho}{\rho_0})^\gamma$  [43]:

$$V_{\text{asy}}^{(2)}(\rho, \delta) = \left[ E_0(\rho_0)(\gamma - 1) \left( \frac{\rho}{\rho_0} \right)^\gamma + 4.2 \left( \frac{\rho}{\rho_0} \right)^{2/3} \right] \times \delta^2 + \left( E_0(\rho_0) \left( \frac{\rho}{\rho_0} \right)^\gamma - 12.7 \left( \frac{\rho}{\rho_0} \right)^{2/3} \right) \delta \tau^{n(p)}, \quad (14)$$

where  $\tau^n = 1$ ,  $\tau^p = -1$ ,  $E_0(\rho_0)$  is set to 30 MeV in this paper, and parameter  $\gamma$  represents the stiffness of the symmetry energy. In the following, we consider two cases of  $\gamma = 0.5$

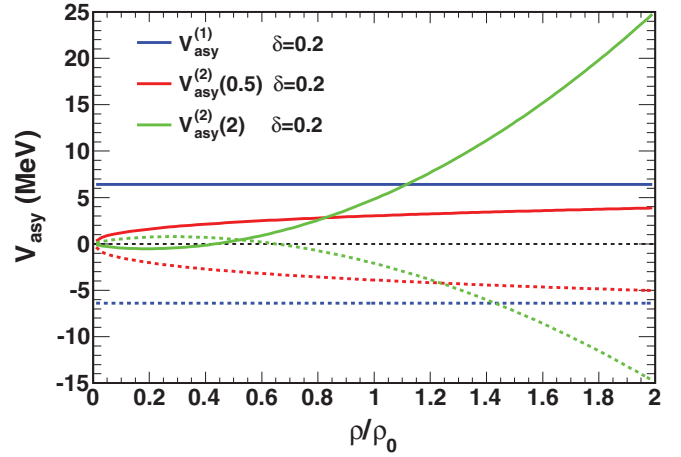


FIG. 13. (Color online) Different symmetry potentials used in the present model calculation as a function of density for an isospin asymmetry of  $\delta = 0.2$  and  $\gamma$  parameters of 0.5 (red line) and 2.0 (green line), respectively. Solid lines are for neutrons and dashed lines are for protons.

and 2, respectively, corresponding to soft and stiff symmetry energy, to explore the effects of different symmetry potential.

The symmetry potentials for neutrons and protons with  $\delta = 0.20$  are plotted in Fig. 13, where the red line represents  $V_{\text{asy}}^{(1)}$ , and the blue and green lines represent  $V_{\text{asy}}^{(2)}$  for  $\gamma$  parameters of 0.5 and 2.0 for neutrons (upper branch) and protons (lower branch), respectively. For small isospin asymmetry and density near  $\rho_0$  the above symmetry potentials reduce to the well-known Lane potential, which varies linearly with  $\delta$  [44]. Generally, the repulsive (attractive) symmetry potential for neutrons (protons) increases with density.

Figure 14 shows the time evolution of inclusive hard-photon multiplicity in the reaction  $^{48}\text{Ca} + ^{48}\text{Ca}$  at 60A MeV. In order to separate the effects of symmetry potential from the incompressibility, we set  $K$  as a constant 380 MeV. Figure 14 presents the effects of different symmetry potentials on hard-photon production. As with the incompressibility  $K$ , direct-photon production is insensitive to the symmetry potential at the studied reaction energy. For thermal photons, the curves of  $V_{\text{asy}}^{(0)}$  and  $V_{\text{asy}}^{(1)}$  have nearly the same multiplicities with time evolution, and they are intermediate between  $V_{\text{asy}}^{(2)(0.5)}$  and  $V_{\text{asy}}^{(2)(2)}$ . We note that thermal-photon production is sensitive to the  $\gamma$  parameter in the symmetry potential  $V_{\text{asy}}^{(2)}(\gamma)$ , i.e., a lower  $\gamma$ , corresponding to softer symmetry energy, induces more thermal photons. And we also note that the sensitivity of thermal-photon production to  $\gamma$  is not remarkable in comparison with its sensitivity to the incompressibility  $K$ , which is, of course, understandable since the symmetry energy is a relatively small term in comparison with the incompressibility  $K$ .

From the effects of the incompressibility and symmetry potential on hard-photon production, it appears that the yield of thermal photons has a rather strong dependence on nuclear compressibility as well as symmetry energy, whereas the yield of direct photons is rather insensitive to nuclear EOS. Therefore thermal hard photons could serve as a probe of nuclear EOS in intermediate-energy HIC.

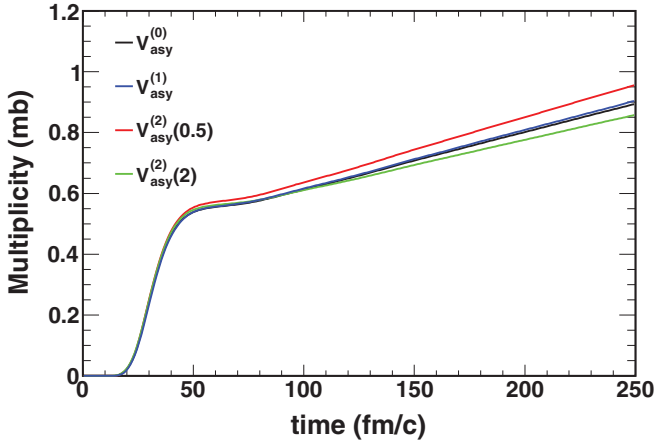


FIG. 14. (Color online) Time evolution of hard-photon multiplicity with different symmetry potentials for the reaction  $^{48}\text{Ca} + ^{48}\text{Ca}$  at 60A MeV.

## V. PHOTON-PHOTON CORRELATIONS

In the above sections, we mainly focus on the properties of inclusive hard photons, from which we find that the production distribution and anisotropic flows of hard photons reveal rich information on nuclear dynamics. Also, the sensitivity to the nuclear equation of state and symmetry energy for hard photons has been discussed. In this section, we will discuss the correlation properties of photons in terms of a two-particle correlation technique that can provide us with a very powerful tool to characterize the properties of a particle source. In particular, two-boson relative momentum distributions enable one to determine the space-time structure according to the formalism of Bose-Einstein correlations. The magnitude of the correlation can be related to their space-time distribution of the boson source. In the following calculations, we will construct a two-photon momentum correlation function as well as an azimuthal correlation function, from which the space-time structure of the photon source and its anisotropy can be indicated.

### A. Two-photon momentum correlation

Intensity interferometry (also called the HBT correlation) is used as a universal tool to study the properties of boson sources such as stars [45] or photon and meson sources in the early phase of heavy-ion collisions [46]. The formalism was developed starting from optics and quantum statistics and was finally adapted to the dynamics of heavy-ion collisions [47–55]. We have performed the calculation which evaluates the correlation function directly from the photon source distribution given by the BUU calculation. We store for each  $i$ th  $pn$  collision its position  $\vec{r}_i$  and the associated photon probability distribution  $P_i(\vec{k}_i)$ . After the completion of the calculation, we analyze the output data to construct plane waves with four-momentum  $\vec{k}_i$  at  $\vec{r}_i$  and calculate the two-photon probability for  $i \neq j$  as [38,56]

$$P_{12} = P_{1 \otimes 2} |A e^{i(\vec{k}_1 \cdot \vec{r}_i + \vec{k}_2 \cdot \vec{r}_j)} + B e^{i(\vec{k}_1 \cdot \vec{r}_j + \vec{k}_2 \cdot \vec{r}_i)}|^2 \quad (15)$$

$$= P_{1 \otimes 2} [1 + 2AB \cos[q(\vec{r}_i - \vec{r}_j)]], \quad (16)$$

where  $P_{1 \otimes 2}$  represents the probability to produce a pair without correlation, and  $A$  and  $B$  are the amplitudes related to the normalized probabilities of the direct [ $P_i(\vec{k}_1)P_j(\vec{k}_2)$ ] and cross terms [ $P_j(\vec{k}_1)P_i(\vec{k}_2)$ ]. This corresponds to Fourier-transforming the photon source event by event. We set the weight of the interference in Eq. (16) as  $\kappa$ , that is,  $\kappa = 2AB$ , which was predicted between 0.5 and 1.0 depending on the anisotropy of hard-photon emission. The exact experimental filter was finally applied to the projection onto the Lorentz-invariant relative four-momentum  $Q = \sqrt{\mathbf{q}^2 - q_0^2}$  of the resulting distribution  $P_{12}$  and  $P_{1 \otimes 2}$  of Eq. (16), then the two-photon correlation function was calculated as  $C_{12}(Q) = \frac{P_{12}}{P_{1 \otimes 2}} = 1 + \kappa \cos[q(\vec{r}_i - \vec{r}_j)] = f(Q)$ .

For convenience,  $\kappa$  was set to 0.75 for our calculations in order to take into account the established anisotropic component in the angular distribution of hard photons. The two-photon correlation function has been fitted with a Gaussian parametrization with correlation strength  $\lambda$  and radius parameter  $R_Q$ :

$$C_{12} = 1 + \lambda \exp(-Q^2 R_Q^2). \quad (17)$$

In the above relation  $R_Q$  is the space-time parameter conjugate to  $Q$ , which measures an invariant length depending on the source-size parameters  $R$  and  $\tau$ :

$$R_Q = R \sqrt{\frac{1 + (\tau/R)^2 (q_0/q)^2}{1 - (q_0/q)^2}}. \quad (18)$$

One can easily see that, since  $q_0 \ll q$ ,  $R_Q$  is a first-order measure of the spatial extent of the source, that is,  $R \approx R_Q$ . We can then calculate from  $R_Q$  the rms radius of the source as one of a static three-dimensional Gaussian source:  $R_{\text{rms}} = \sqrt{3}R_Q$ .

For the comparisons with experimental data, we calculated the reaction  $^{86}\text{Kr} + ^{58}\text{Ni}$  at 60A MeV, employing here the following filter, which is very similar to the experiment:  $E_\gamma(1, 2) > 25$  MeV, detector positions between polar angles of  $35^\circ$  and  $165^\circ$  (oriented downstream), azimuthal opening angles of  $0^\circ \pm 28^\circ$  and  $180^\circ \pm 28^\circ$ , and  $18^\circ$  for the minimum opening angle. Figure 15 presents HBT correlation functions of direct photons (green squares), thermal photons (blue triangles), and inclusive photons (red open circles), respectively. We find that the correlation function of direct photons is much larger than that for thermal ones, and the correlation function of inclusive photons is intermediate. This result is reasonable, because direct photons are emitted at the early compressed stage of collisions, so they interfere more strongly than thermal photons, which are produced in the later thermalizing stage. We also see that our result can well reproduce the experimental data [38,39], especially for the correlation function of thermal photons, which agrees with the experimental function, even for the oscillation structure. Therefore, we can successfully reproduce the HBT correlation function of hard photons by the BUU simulation.

In order to further study the HBT correlation of hard photons and extract photon source information, we calculated the symmetric reaction system  $^{40}\text{Ca} + ^{40}\text{Ca}$  at 60A MeV in the c.m. frame, and only the events of central collision



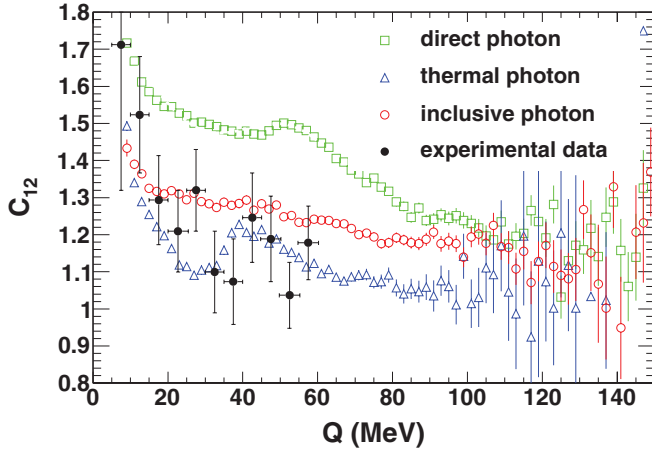


FIG. 15. (Color online) Two-photon HBT correlation function for  $^{86}\text{Kr} + ^{58}\text{Ni}$  collisions at 60A MeV in the laboratory frame, with  $E_\gamma > 25$  MeV. The green squares represent direct photons, blue triangles are for thermal photons, and red open circles are for inclusive photons. The black closed circles represent the experimental data taken from Refs. [38,39].

( $0 < b_{\text{red}} \leq 0.2$ ) were taken for simplification. In Fig. 16, we find that the correlation function of direct photons is the largest, that of the thermal ones is the least, and the correlation function of inclusive photons are in between these. Moreover, in the conditions of the above reaction, all of them can be well fitted by Eq. (17). After fitting the correlation function, we can obtain two useful fitting parameters: correlation strength  $\lambda$  and radius parameter  $R_Q$ . As the results in the top right corner show, direct photons have the largest correlation strength  $\lambda$ , the second largest is from inclusive photons, and thermal photons have the least. Thus  $\lambda$  is a parameter which is sensitive to the intensity of interference. And we also get three radius parameters  $R_Q$ . The radius  $R_Q$  of thermal photons is nearly twice that of direct photons, and that of inclusive photons is equivalent to the later. To explain this, we note that direct photons are mostly

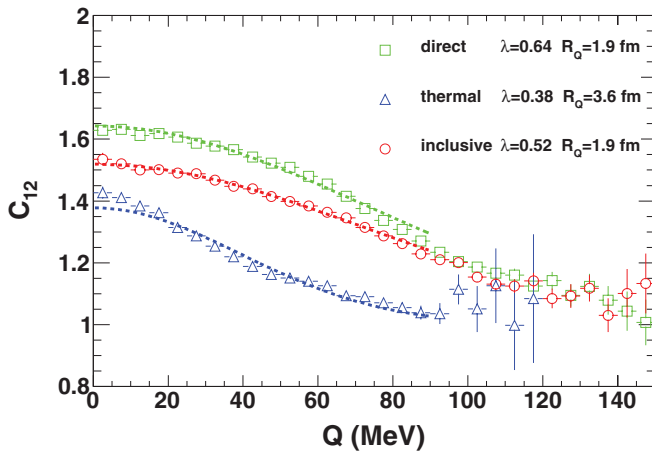


FIG. 16. (Color online) Two-photon HBT correlation function for  $^{40}\text{Ca} + ^{40}\text{Ca}$  collisions at 60A MeV. The symbols are the same as Fig. 15 and the dashed lines are the fitting functions from Eq. (17).

emitted in the early stage when the reaction system is strongly compressed, so the emission source of photons is small. Later on, the thermalizing system extends very much in company with the production of thermal photons. In this reaction at  $E_{\text{lab}} = 60A$  MeV, most of the hard photons are produced in the early stage of the collision, so the spatial source extent of inclusive photons should be approximate to that of the direct photons. As a result, they have equivalent radius parameter  $R_Q$ . Then we can get the rms radius of the photon source by the equation  $R_{\text{rms}} = \sqrt{3}R_Q$ . Therefore, the two-photon correlation function provides information on the hard-photon source, which is available to investigate the emission source during the collisions.

## B. Two-photon azimuthal correlation

From the individual-photon azimuthal distribution, we find that direct hard photons exhibit azimuthal asymmetric emission in intermediate-energy heavy-ion collisions, especially for the negative elliptic flow parameter  $v_2$ . Actually, it is difficult to extract the elliptic flow parameter  $v_2$  by the method of reconstructing the reaction plane in the experiment, so, below, we will discuss using the two-photon azimuthal correlation method to extract the elliptic flow of direct photons directly.

For particles in the same class, we defined the particle azimuthal correlation function following the multifragment azimuthal correlation method [29,57,58]. The multifragment azimuthal correlation function is defined as follows:

$$C(\Delta\phi) = \frac{N_{\text{cor}}(\Delta\phi)}{N_{\text{uncor}}(\Delta\phi)}, \quad (19)$$

where  $N_{\text{cor}}$  is the  $\Delta\phi$  distribution for fragment pairs from the same event and  $N_{\text{uncor}}$  is the  $\Delta\phi$  distribution by randomly selecting each member of a fragment pair to form mixed events. The  $\Delta\phi$  values between all selected fragments in an event are used to construct the correlation function, that is,  $\frac{n(n-1)}{2}\Delta\phi$  angles for  $n$  fragments.

In our calculations for two-photon azimuthal correlations, we get  $N_{\text{cor}}$  from the  $\Delta\phi$  distribution of photon pairs in the same event and  $N_{\text{uncor}}$  from the mixed events. For these correlations, we may make a fit of the Fourier series with the expression

$$C(\Delta\phi) = A[1 + \lambda_1 \cos(\Delta\phi) + \lambda_2 \cos(2\Delta\phi)], \quad (20)$$

where  $\lambda_1$  and  $\lambda_2$  are treated as fit parameters.

Under the assumption of statistically independent emission of particles with the same azimuthal distribution  $F(\phi)$  in an event, the azimuthal correlation function is simply related to  $F(\phi)$  via the convolution

$$C(\Delta\phi) = \int_0^{2\pi} F(\phi)F(\phi + \Delta\phi)d\phi. \quad (21)$$

On the other hand,  $F(\phi)$  can be described by the Fourier expansion

$$F(\phi) = \frac{dN}{d\phi} \propto 1 + 2 \sum_{n=1}^{\infty} v_n \cos(n\phi), \quad (22)$$

where the different  $n$ th harmonic Fourier expansion coefficients  $v_n$  are defined for the  $n$ th anisotropic flow, of which  $v_1$

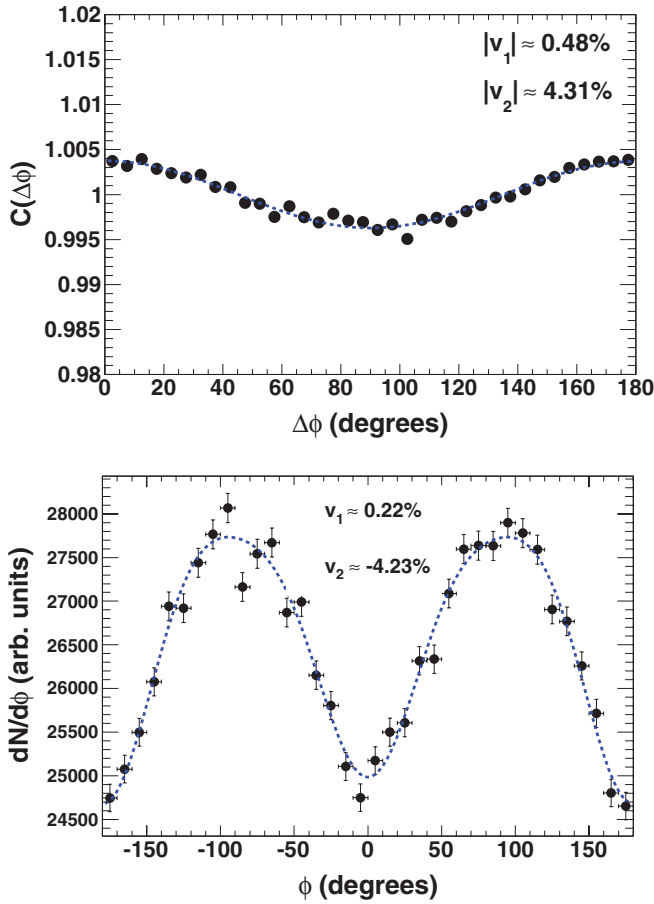


FIG. 17. (Color online) Top panel: Two-photon azimuthal correlation function for the reaction  $^{40}\text{Ca} + ^{40}\text{Ca}$  at 60A MeV for semicentral events (40%–60%); the dashed line is the fitting function from Eq. (20). Bottom panel: Individual-photon azimuthal distribution for the same reaction; the dashed line is a fit of a Fourier expansion.

is the directed flow parameter and  $v_2$  is the so-called elliptic flow parameter.

If we only take  $v_1$  and  $v_2$  terms in Eq. (22) and substitute Eq. (22) into Eq. (21), we can derive the form of  $C(\Delta\phi)$  as follows:

$$C(\Delta\phi) = B[1 + 2v_1^2 \cos(\Delta\phi) + 2v_2^2 \cos(2\Delta\phi)] \quad (23)$$

From Eqs. (21) and (22), we then get the relationship between the fitted parameter  $\lambda_2$  and the elliptic flow parameter  $v_2$  [29]:

$$|v_2| \approx \sqrt{\lambda_2/2}. \quad (24)$$

Now we make the comparison of the elliptic flow parameter  $v_2$  extracted from the two-photon azimuthal correlation with a fitting value from the individual-photon azimuthal distribution. In Fig. 17, we calculated the reaction  $^{40}\text{Ca} + ^{40}\text{Ca}$  at 60A MeV for semicentral events (40%–60%) with compressibility  $K = 235$  MeV, and we extracted the elliptic flow parameters  $v_2$  by the two distinct methods above. Then we can see that the absolute values of  $v_2$  are nearly equivalent, except that we can only get the amplitude of the elliptic flow from the two-photon azimuthal correlation, and the fitting value of  $v_2$  from the

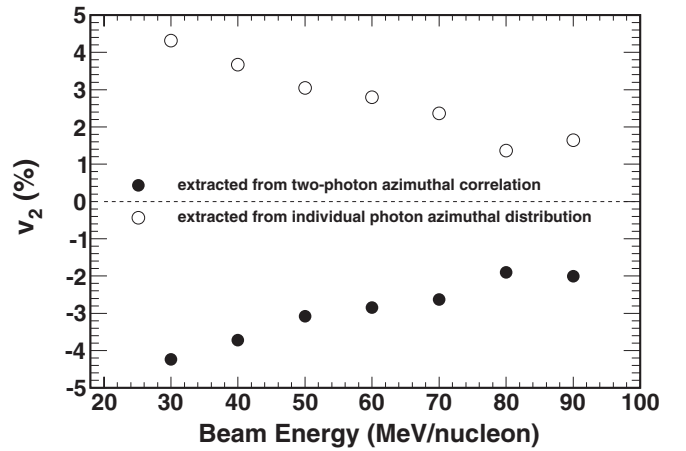


FIG. 18. Excitation function of  $v_2$  for reaction  $^{40}\text{Ca} + ^{40}\text{Ca}$  at 60A MeV with centrality 40%–60%. Open circles represent the amplitude of  $v_2$  extracted from the two-photon azimuthal correlation and red ones are from a fit of a Fourier expansion to the individual-photon azimuthal distribution.

individual-photon azimuthal distribution is negative. Further, as shown in Fig. 18, the excitation functions of  $v_2$  obtained by the above two methods show nearly the same amplitude of  $v_2$  at various reaction energies but are of different signs. Therefore, in view of the difficulty in reconstructing the reaction plane in the experiment, the two-photon azimuthal correlation provides us with an alternative method for extracting the amplitude of the elliptic flow parameter  $v_2$  of hard photons.

## VI. SUMMARY

In summary, we have systematically investigated hard-photon production by the process of proton-neutron bremsstrahlung as well as the behavior of azimuthal asymmetry of hard photons and free protons produced in intermediate-energy heavy-ion collisions in the framework of the BUU model. As discussed in previous studies, hard photons can be separated into direct hard photons, which are produced by the first-channel neutron-proton bremsstrahlung, and thermal hard photons, which are produced by the later-stage neutron-proton bremsstrahlung during the system's evolution toward thermalization. The kinetic energy spectra of these two kinds of photons show an exponential form which provides us with information on the apparent temperature in different stages of heavy-ion collision.

The azimuthal asymmetry parameters have been investigated in detail. The time evolution of directed flow and elliptic flow of hard photons exhibits a rich structure as the density of the system oscillates during the preequilibrium and thermalization stages of the reaction system. This structure indicates that the azimuthal asymmetry evolves with time. A nonzero directed transverse flow and elliptic flow parameter have been predicted for the direct hard photons produced by the first-channel proton-neutron bremsstrahlung process in the intermediate-energy heavy-ion collisions. The asymmetry parameters of hard photons are plotted as a function of rapidity and transverse momentum, which show contrary signs in

comparison with the flow of free protons; i.e., the azimuthal asymmetry of direct hard photons seems to be anticorrelated to that of the corresponding free protons. Therefore we can expect the direct hard photon can serve as a good probe of nuclear matter properties in the early stage of HIC.

Different variables dependencies are investigated for the hard-photon production and anisotropic flow. We can see that the absolute values of both directed flow and elliptic flow of direct photons and free protons increase with the impact parameter, indicating that the flow mainly reflects the initial geometric asymmetry of the collision zone in a given beam energy and revealing a rich structure of flows with increasing beam energy. For directed flow, direct photons reach a minimum of around 40A MeV where the free protons approach the maximum negative value, while for elliptic flow, the absolute values of direct photons show decreasing trends with increasing beam energy. The EOS dependence for hard photons at different times indicates that the direct photon is not sensitive to the nuclear incompressibility nor to the symmetry energy. However, for the thermal photon, its multiplicity increases with nuclear incompressibility. For a given nuclear incompressibility, the soft symmetry energy favors thermal-photon production.

Finally, we calculated the two-photon correlations, including HBT momentum correlations and azimuthal correlations. From two-photon HBT correlations, we can extract photon source information, such as intensity interference and the spatial extent of the emission source. We also find that two-photon azimuthal correlations can provide us with a good method for extracting the amplitude of the elliptic flow parameter  $v_2$  of hard photons in the experiment.

In light of the present study, we expect that direct photons would be a very useful probe for exploring nuclear reaction dynamics in intermediate-energy heavy-ion collisions, while the thermal hard photon can give us some hints on the nuclear EOS, including the symmetry energy.

### ACKNOWLEDGMENTS

This work is supported partially by the Knowledge Innovation Project of the Chinese Academy of Sciences under Grant No. KJCX2-EW-N01 and the National Natural Science Foundation of China under Contracts No. 11035009, No. 11005140, No. 10979074, No. 10875160, No. 10805067, and No. 10975174.

- 
- [1] Y. Schutz, G. Martínez, F. M. Marqués, A. Marín, T. Matulewicz, R. W. Ostendorf P. Božek, H. Delagrange, J. Díaz, M. Franke, K. K. Gudima, S. Hlaváč, R. Holzmann, P. Lautridou, F. Lefèvre, H. Löhner, W. Mittig, M. Płoszajczak, J. H. G. van Pol, J. Québert, P. Roussel-Chomaz, A. Schubert, R. H. Siemssen, R. S. Simon, Z. Sujkowski, V. D. Toneev, V. Wagner, H. W. Wilschut, and G. Wolf, *Nucl. Phys. A* **622**, 404 (1997).
- [2] W. Cassing, V. Metag, U. Mosel, and K. Niita, *Phys. Rep.* **188**, 363 (1990).
- [3] A. Bonasera, R. Coniglione, and P. Sapienza, *Eur. Phys. J. A* **30**, 47 (2006).
- [4] H. Nifenecker and J. A. Pinston, *Annu. Rev. Nucl. Part. Sci.* **40**, 113 (1990).
- [5] R. Wada, D. Fabris, K. Hagel, G. Nebbia, Y. Lou, M. Gonin, J. B. Natowitz, R. Billerey, B. Cheynis, A. Demeyer, D. Drain, D. Guinet, C. Pastor, L. Vagneron, K. Zaid, J. Alarja, A. Giorni, D. Heuer, C. Morand, B. Viano, C. Mazur, C. Ng, S. Leray, R. Lucas, M. Ribrag, and E. Tomasi, *Phys. Rev. C* **39**, 497 (1989).
- [6] Y. Schutz *et al.* (TAPS Collaboration), *Nucl. Phys. A* **599**, 97 (1996).
- [7] Y. Schutz *et al.* (TAPS Collaboration), *Nucl. Phys. A* **630**, 126 (1998).
- [8] G. Martínez, F. M. Marqués, Y. Schutz, G. Wolf, J. Díaz, M. Franke, S. Hlaváč, R. Holzmann, P. Lautridou, F. Lefèvre, H. Löhner, A. Marín, T. Matulewicz, W. Mittig, R. W. Ostendorf, J. H. G. van Pol, J. Québert, P. Roussel-Chomaz, A. Schubert, R. H. Siemssen, R. S. Simon, Z. Sujkowski, V. Wagner, and H. W. Wilschut, *Phys. Lett. B* **349**, 23 (1995).
- [9] D. G. d'Enterria, L. Aphecetche, A. Chbihi, H. Delagrange, J. Díaz, M. J. van Goethem, M. Hoefman, A. Kugler, H. Löhner, G. Martínez, M. J. Mora, R. Ortega, R. W. Ostendorf, S. Schadmand, Y. Schutz, R. H. Siemssen, D. Stracener, P. Tlustý, R. Turrisi, M. Volkerts, V. Wagner, H. W. Wilschut, and N. Yahlali, *Phys. Rev. Lett.* **87**, 022701 (2001).
- [10] A. Adare *et al.* (PHENIX Collaboration), *Phys. Rev. Lett.* **104**, 132301 (2010).
- [11] J. L. Long, Z. J. He, Y. G. Ma, and B. Liu, *Phys. Rev. C* **72**, 064907 (2005); *Nucl. Phys. A* **766**, 201 (2006).
- [12] F. M. Liu, T. Hirano, K. Werner, and Y. Zhu, *Phys. Rev. C* **79**, 014905 (2009).
- [13] M. M. Aggarwal *et al.* (WA98 Collaboration), *Phys. Rev. Lett.* **85**, 3595 (2000).
- [14] W. Bauer, G. F. Bertsch, W. Cassing, and U. Mosel, *Phys. Rev. C* **34**, 2127 (1986).
- [15] G. F. Bertsch, S. Das Gupta, *Phys. Rep.* **160**, 189 (1988).
- [16] J. D. Jackson, *Classical Electrodynamics* (Wiley, New York, 1962), p. 733.
- [17] W. Cassing, T. Biro, U. Mosel, M. Tohyama, and W. Bauer, *Phys. Lett. B* **181**, 217 (1986).
- [18] G. H. Liu, Y. G. Ma, X. Z. Cai, D. Q. Fang, W. Q. Shen, W. D. Tian, and K. Wang, *Phys. Lett. B* **663**, 312 (2008).
- [19] F. M. Marqués, G. Martínez, Y. Schutz, J. Díaz, M. Franke, S. Hlaváč, R. Holzmann, P. Lautridou, F. Lefèvre, H. Löhner, A. Marín, T. Matulewicz, W. Mittig, R. W. Ostendorf, J. H. G. van Pol, J. Québert, P. Roussel-Chomaz, A. Schubert, R. H. Siemssen, R. S. Simon, Z. Sujkowski, V. Wagner, H. W. Wilschut, and G. Wolf, *Phys. Lett. B* **349**, 30 (1995).
- [20] A. Corsi, O. Wieland, V. L. Kravchuk, A. Bracco, F. Camera, G. Benzoni, N. Blasi, S. Brambilla, F. C. L. Crespi, A. Giussani, S. Leoni, B. Million, D. Montanari, A. Moroni, F. Gramegna, A. Lanchais, P. Mastinu, M. Brekiesz, M. Kmiecik, A. Maj, M. Bruno, M. D'Agostino, E. Geraci, J. G. Vannini, S. Barlini, G. Casini, M. Chiari, A. Nannini, A. Ordine, M. Di Toro, C. Rizzo, M. Colonna, and V. Barank, *Phys. Lett. B* **679**, 197 (2009).
- [21] V. Baran, C. Rizzo, M. Colonna, M. Di Toro, and D. Pierrousakou, *Phys. Rev. C* **79**, 021603 (2009).
- [22] H. L. Wu, W. D. Tian, Y. G. Ma, X. Z. Cai, J. G. Chen, D. Q. Fang, W. Guo, and H. W. Wang, *Phys. Rev. C* **81**, 047602 (2010).

- [23] A. Bonasera, F. Gulminelli, and J. Molitoris, *Phys. Rep.* **243**, 1 (1994).
- [24] J. Y. Ollitrault, *Phys. Rev. D* **46**, 229 (1992).
- [25] S. Voloshin and Y. Zhang, *Z. Phys. C* **70**, 665 (1996).
- [26] H. Sorge, *Phys. Lett. B* **402**, 251 (1997); *Phys. Rev. Lett.* **78**, 2309 (1997); **82**, 2048 (1999).
- [27] P. Danielewicz, R. A. Lacey, P. B. Gossiaux, C. Pinkenburg, P. Chung, J. M. Alexander, and R. L. McGrath, *Phys. Rev. Lett.* **81**, 2438 (1998).
- [28] Y. G. Ma, W. Q. Shen, J. Feng, and Y. Q. Ma, *Phys. Rev. C* **48**, R1492 (1993); *Z. Phys. A* **344**, 469 (1993); Y. G. Ma, W. Q. Shen, and Z. Y. Zhu, *Phys. Rev. C* **51**, 1029 (1995); *Nucl. Phys. A* **787**, 611c (2007).
- [29] Y. G. Ma and W. Q. Shen, *Phys. Rev. C* **51**, 3256 (1995).
- [30] Y. M. Zheng, C. M. Ko, B. A. Li, and B. Zhang, *Phys. Rev. Lett.* **83**, 2534 (1999).
- [31] D. Persram and C. Gale, *Phys. Rev. C* **65**, 064611 (2002).
- [32] J. Łukasiak *et al.* (INDRA and ALDAIN Collaboration), *Phys. Lett. B* **608**, 223 (2004).
- [33] T. Z. Yan, Y. G. Ma, X. Z. Cai, J. G. Chen, D. Q. Fang, W. Guo, C. W. Ma, E. J. Ma, W. Q. Shen, W. D. Tian, and K. Wang, *Phys. Lett. B* **638**, 50 (2006).
- [34] J. H. Chen, Y. G. Ma, G. L. Ma, X. Z. Cai, Z. J. He, H. Z. Huang, J. L. Long, W. Q. Shen, C. Zhong, and J. X. Zuo, *Phys. Rev. C* **74**, 064902 (2006).
- [35] M. M. Aggarwal *et al.* (WA98 Collaboration), *Phys. Rev. Lett.* **93**, 022301 (2004); *Nucl. Phys. A* **762**, 129 (2005).
- [36] S. S. Adler *et al.* (PHENIX Collaboration), *Phys. Rev. Lett.* **96**, 032302 (2006).
- [37] S. Turbide, C. Gale, and R. J. Fries, *Phys. Rev. Lett.* **96**, 032303 (2006).
- [38] H. W. Barz, B. Kampfer, G. Wolf, and W. Bauer, *Phys. Rev. C* **53**, R553 (1996).
- [39] F. M. Marques, G. Martinez, T. Matulewicz, R. W. Ostendorf, and Y. Schutz, *Phys. Rev. C* **54**, 2783 (1996).
- [40] V. Herrmann, J. Speth, and K. Nakayama, *Phys. Rev. C* **43**, 394 (1991).
- [41] Y. Safkan, T. Akdogan, W. A. Franklin, J. L. Matthews, W. M. Schmitt, V. V. Zelevinsky, P. A. M. Gram, T. N. Taddeucci, S. A. Wender, and S. F. Pate, *Phys. Rev. C* **75**, 031001 (2007).
- [42] H. Heiselberg and M. Hjorth-Jensen, *Phys. Rep.* **328**, 237 (2000).
- [43] B. A. Li, A. T. Sustich, and B. Zhang, *Phys. Rev. C* **64**, 054604 (2001).
- [44] A. M. Lane, *Nucl. Phys. A* **35**, 676 (1962).
- [45] R. Hanbury-Brown and R. Q. Twiss, *Philos. Mag.* **45**, 663 (1954).
- [46] G. Goldhaber, S. Goldhaber, W. Lee, and A. Pais, *Phys. Rev.* **120**, 300 (1960).
- [47] B. Lörstad, *Int. J. Mod. Phys. A* **4**, 2861 (1989).
- [48] D. H. Boal, C. K. Gelbke, and B. K. Jennings, *Rev. Mod. Phys.* **62**, 553 (1990).
- [49] J. Québert, *Ann. Phys. (Paris)* **17**, 99 (1992).
- [50] S. E. Koonin, *Phys. Lett. B* **70**, 43 (1977).
- [51] S. Pratt, *Phys. Rev. Lett.* **53**, 1219 (1984).
- [52] W. G. Lynch, C. B. Chitwood, M. B. Tsang, D. J. Fields, D. R. Klesch, C. K. Gelbke, G. R. Young, T. C. Awes, R. L. Ferguson, F. E. Obenshain, F. Plasil, R. L. Robinson, and D. Panagiotou, *Phys. Rev. Lett.* **51**, 1850 (1983).
- [53] F. M. Marques, G. Martinez, T. Matulewicz, R. W. Ostendorf, and Y. Schutz, *Phys. Rep.* **284**, 91 (1997).
- [54] Y. B. Wei, Y. G. Ma, W. Q. Shen, G. L. Ma, K. Wang, X. Z. Cai, C. Zhong, W. Guo, and J. G. Chen, *Phys. Lett. B* **586**, 225 (2004).
- [55] Y. G. Ma, Y. B. Wei, W. Q. Shen, X. Z. Cai, J. G. Chen, J. H. Chen, D. Q. Fang, W. Guo, C. W. Ma, G. L. Ma, Q. M. Su, W. D. Tian, K. Wang, T. Z. Yan, C. Zhong, and J. X. Zuo, *Phys. Rev. C* **73**, 014604 (2006); Y. G. Ma, X. Z. Cai, J. G. Chen, D. Q. Fang, W. Guo, G. H. Liu, C. W. Ma, E. J. Ma, W. Q. Shen, Y. Shi, Q. M. Su, W. D. Tian, H. W. Wang, K. Wang, Y. B. Wei, and T. Z. Yan, *Nucl. Phys. A* **790**, 299c (2007).
- [56] M. Marqués, R. W. Ostendorf, P. Lautridou, F. Lefèvre, T. Matulewicz, W. Mittag, P. Roussel-Chomaz, Y. Schutz, J. Québert, J. Díaz, A. Marín, G. Martínez, R. Holzmann, S. Hlávač, A. Schubert, R. S. Simon, V. Wagner, H. Löhner, J. H. G. van Pol, R. H. Siemssen, H. W. Wilschut, M. Franke, and Z. Sujkowski, *Phys. Rev. Lett.* **73**, 34 (1994); F. M. Marqués, G. Martinez, T. Matulewicz, R. W. Ostendorf, and Y. Schutz, *Phys. Rev. C* **54**, 2783 (1996).
- [57] S. Wang, Y. Z. Jiang, Y. M. Liu, D. Keane, D. Beavis, S. Y. Chu, S. Y. Fung, M. Vient, C. Hartnack, and H. Stöcker, *Phys. Rev. C* **44**, 1091 (1991).
- [58] R. A. Lacey, A. Elmaani, J. Lauret, T. Li, W. Bauer, D. Craig, M. Cronqvist, E. Gualtieri, S. Hannuschke, T. Reposeur, A. Vander Molen, G. D. Westfall, W. K. Wilson, J. S. Winfield, J. Yee, S. Yennello, A. Nadasen, R. S. Tickle, and E. Norbeck, *Phys. Rev. Lett.* **70**, 1224 (1993).